Trajectory-Aided Maximum-Likelihood Algorithm for Channel Parameter Estimation in Ultra-Wideband Large-Scale Arrays

Cai, Xuesong; Fan, Wei; Yin, Xuefeng; Pedersen, Gert Frølund

Published in:
IEEE Transactions on Antennas and Propagation

DOI (link to publication from Publisher):
10.1109/TAP.2020.2996774

Publication date:
2020

Document Version
Accepted author manuscript, peer reviewed version

Trajectory-Aided Maximum-Likelihood Algorithm for Channel Parameter Estimation in Ultra-Wideband Large-Scale Arrays

Xuesong Cai, Wei Fan, Xuefeng Yin, and Gert Frølund Pedersen

***Abstract*—Millimeter-wave with ultra-wide bandwidth available and ability to pack massive number of antennas in a small area is considered the key enabler for the future generation communication systems. Accurate understanding and modeling of the ultra-wideband propagation channel with large-scale array configuration is essential. In this contribution, a realistic spherical-propagation signal model considering the spatial non-stationarity of path gain across the array elements is proposed. A novel Trajectory-Aided Maximum-likelihood (TAMax) algorithm is proposed to extract propagation parameters from the measured data, since the existing high-resolution propagation parameter estimation algorithms are not applicable due to either prohibitively high computation loads or assumption violations. In the proposed TAMax algorithm, the high-dimensional Maximum-Likelihood (ML) estimation problem is firstly decomposed into a sub-problem where delays and amplitudes of MultiPath Components (MPCs) are estimated at individual array elements. A novel transform is then proposed to identify multiple MPC trajectories in the delay-element domain. With interference cancellation and fast initialization obtained in the proposed transform, spherical propagation parameters are finally acquired via joint ML estimation with significantly decreased searching spaces. Moreover, a measurement campaign conducted at the frequency band of 27-29 GHz using a virtual uniform circular array is introduced, where the proposed TAMax algorithm is applied and validated.**

***Index terms*—** Millimeter-wave, spherical wave propagation, spatial non-stationarity, large-scale array, and ultra-wideband.

I. Introduction

The next fifth-generation communication system (5G) is expected to significantly improve the network capacity, data rates and latency with greatly increased network flexibility and efficiency while at the similar cost and energy dissipation as today [1]. The prospect is expected to be provided by increased bandwidth, massive Multiple-Input-Multiple-Output (MIMO), multi-user MIMO, new modulation waveforms, network densification, etc. [2]. Since the bandwidth increase can give the most direct capacity increase, millimeter-wave (mmWave) with vast amount of available spectrum [3], [4] has been considered the key enabler for 5G. Moreover, the small wavelength of mmWave makes it practically feasible to realize a large-scale antenna array in a small area [5]. Further, the interference among densified small cells can be decreased by the high power loss [6] of mmWave. To design advanced techniques and evaluate system performance for the future communication systems, it is vital to establish realistic channel models for ultra-wideband communications in mmWave bands with large-scale array configuration.

A. Channel characteristics

Measurement campaigns are indispensable to establish realistic models for the ultra-wideband mmWave propagation channel. Propagation channel parameters can then be extracted from the measurement data for further investigations on channel properties. Compared with that of the sub-6 GHz frequency bands, the mmWave propagation channel measured using sounding signals with ultra-wide bandwidth and large-scale array configuration mainly has the following new aspects that need to be carefully considered.[1] First, the large bandwidth of the sounding signals (up to several GHz) significantly improves the delay resolution, hence the ability to resolve the Multipath Components (MPCs) in the delay domain. Consequently, the assumption that the sounding signal is narrowband across the array [7] might be violated. That is, the impulse responses of the same path observed at different array elements may "sit" on different delay bins. Second, due to the advances of massive MIMO [8] and network densification [9], distance between a transmitter and a receiver can become much smaller. As a result, propagation paths can have non-negligible elevation angles. Moreover, it has been a consensus that the so-called 3D-beamforming [8] will be the key technology, e.g., to combat human and vehicular blockage loss [10]. Therefore, propagation channel characteristics in the elevation domain have to be carefully considered when conducting measurement campaigns and/or parameter estimations. Third, with the small wavelength and large-scale array aperture, the

The work was partially supported by Huawei technologies, InnoExplorer project (2019 9122-00089A) funded by Innovation Fund Denmark and China National Science Fundation (CNSF) general project with grant number 61971313. (*Corresponding authors: Xuesong Cai and Xuefeng Yin.*)

X. Cai was with the APMS section at the Department of Electronic Systems, the Technical Faculty of IT and Design, Aalborg University, Aalborg 9220, Denmark. The work was conducted when X. Cai was with the APMS section. He is now with the WCN section at the Department of Electronic Systems, the Technical Faculty of IT and Design, Aalborg University, Aalborg 9220, Denmark (e-mail: xuc@es.aau.dk).

W. Fan and Gert Frølund Pedersen are with the APMS section at the Department of Electronic Systems, the Technical Faculty of IT and Design, Aalborg University, Aalborg 9220, Denmark (e-mail: wfa@es.aau.dk; gfp@es.aau.dk).

X. Yin is with the College of Electronics and Information Engineering, Tongji University, Shanghai 201804, China (e-mail: yinxuefeng@tongji.edu.cn).

[1]Note that these new aspects are considered in both channel sounding and communication viewpoints.

spherical wavefront curvature [11], [12] can also be observed.[2] The investigations in [12], [14] have demonstrated that approximating the spherical wavefront by plane-wavefront can lead to severe model mismatch and result in unrealistic understanding of the propagation channels. Fourth, spatial non-stationarity of path gain across the large array aperture can be evident [15]. That is, the power of the same path may vary across the array. Blockage could be an important reason, since the ability of mmWave to diffract around obstacles such as human body and furniture is limited [16]–[18]. To accurately model the mmWave massive MIMO propagation channels, considerable measurement-based efforts are still required. Hence, sophisticated and complexity-efficient High-Resolution propagation Parameter Estimation (HRPE) is vital and in necessity to extract channel parameters from the measurement data.

B. Existing algorithms

Similar to those applied to the sub-6 GHz propagation channels, the estimation algorithms for mmWave channels can be classified into spectra-based ones, subspace-based ones, sparsity-recovery based ones and Maximum-Likelihood (ML) based ones. The widely used spectra-based approach is to obtain the joint angle-delay spectrum from the measurement data by using the so-called Directional Scan Scheme (DSS) with horn antennas [19]–[22]. Although it is simple and straightforward, the horn antenna radiation pattern is embedded in the extracted propagation channel characteristics. A frequency invariant beamformer has been proposed in [23] to estimate joint delay-azimuth spectrum, which is, however, only applicable for Uniform Circular Arrays (UCAs). As representatives of subspace-based algorithms, MUSIC (MUltiple SIgnal Classification), ESPRIT (unitary Estimation of Signal Parameter via Rotational Invariance Techniques) and their variants can also be found in [24]–[28]. The limitations include the deficiency in resolving large number of paths or a high computation load. Sparsity recovery algorithms [29], [30] are developed based on the assumption that the mmWave channel exhibits sparsity in parameter domains (more measurement verifications are still needed [31]). By exploiting specific optimization principles, e.g. the convex optimization, channel characteristics can be recovered.

Before embarking on the ML-based algorithms, the authors would like to summarize that although the above algorithms may have advantages of low complexity, they are deficient in fully extracting the propagation parameters. For example, none of the algorithms has considered the spherical propagation, and some algorithms, e.g. the proposed frequency invariant beamformer in [23], can only extract the delay and azimuth information. Notwithstanding the probably higher complexity, ML-based algorithms are able to fully estimate the parameters that are properly defined in the signal model when compared to the other algorithms. The most widely used ML-based algorithm for sub-6 GHz propagation channel is the Space-Alternating Generalized Expectation-maximization (SAGE) algorithm [32] because of its low complexity. In [14], a HRPE algorithm which is essentially based on the Expectation-Maximization (EM) principle [33] was proposed for spherical mmWave propagation channels, where only one iteration was applied to reduce computation load to a certain degree. However, when applied for the ultra-wideband propagation channels with large-scale array configuration, these ML-based algorithms are not suitable either in theory or practice. The reasons are as follows. As elaborated in Sect. III, the SAGE algorithm is not applicable due to the violation of 2D, narrowed and plane-wave assumptions. As for the algorithms based on the EM principle [14], [33], the computation load is too high due to the high-dimensional joint parameter searching. In the authors' previous work in [34], an ML-based algorithm which is only applicable for UCA was also proposed to overcome the high computation load of the joint ML estimation, wherein the UCA phase-mode technique was exploited.

C. Motivation and contributions

As a critical signal processing tool in measurement-based modeling for propagation channels in mmWave large-scale arrays, sophisticated, accurate and complexity-efficient HRPE algorithm is essential and in necessity. However, to the authors' best knowledge, a generalized complexity-efficient HRPE algorithm which is applicable for a large-scale array in arbitrary array configuration is still missing in the literature. Under such circumstance, a novel trajectory-aided maximum-likelihood (TAMax) algorithm with low computation load is proposed in this paper. The main contributions and novelties include:

- A generic signal model for the spherical propagation channel with an arbitrary array geometry is proposed. The realistic channel characteristics especially the spatial non-stationarity in path gain across the array are included in the proposed signal model. Classical estimation principles, i.e. ML, EM and SAGE, are revisited with their limitations discussed in detail.
- In the proposed TAMax algorithm for channel parameter estimation, the high-dimensional ML problem is intentionally decomposed into a sub-problem at individual array elements, where only delays and complex amplitudes of MPCs are required to be estimated with low complexity. A novel low-complexity transform is then proposed to identify and distinguish the multiple MPC trajectories in the delay-element domain. Moreover, interference cancellations among MPCs and rough parameter initializations for individual MPCs can also be obtained, which results in a low-complexity final ML estimation for all MPC parameters.

[2]It is worth noting that in mmWave frequency bands, there nowadays exist strong practical challenges in making very large antenna arrays work in communication systems due to, e.g., hardware limitation and power consumption. For moderate-size arrays, spherical-wavefront model is not that practically important, and plane-wavefront can serve a good approximation. Nevertheless, large antenna arrays have gained considerable academic interests for 5G and beyond [8], [13] where spherical wavefront assumption is necessary due to significantly increased Fraunhofer distance (see (1)). Moreover, in propagation channel investigation viewpoint, the capabilities of a sounding system usually surpasses the prior channel. In other words, channel sounding campaigns usually exploit an array with a much larger aperture than practical communication systems. To accurately estimate the channel parameters, spherical wavefront has to be considered in this case.

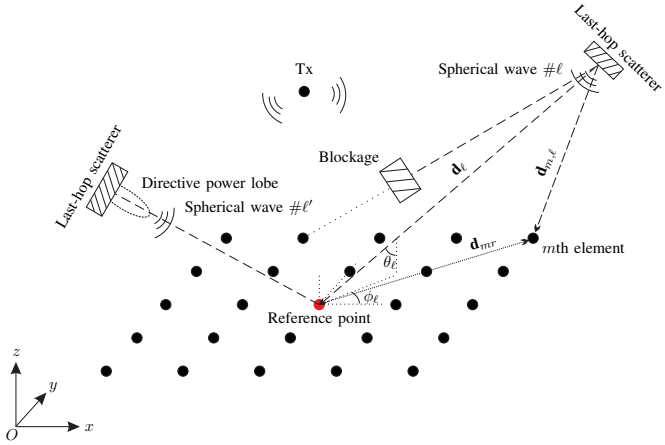

Fig. 1: Spherical-wave propagations with spatial non-stationarity.

- A measurement campaign at the frequency band of 27-29 GHz has been conducted using a UCA with radius of 0.25 m. The spatial non-stationarity in path gain was intentionally produced by the blockage of a metal cylinder. The proposed signal model and the performance of the proposed algorithm are validated by exploiting the measurement data.

The rest of the paper is structured as follows. Sect. II elaborates the signal model and formulates the problem. Important state-of-the-art HRPE algorithms are revisited in Sect. III. Sect. IV elaborates the proposed TAMax algorithm. In Sect. V, the measurement campaign and the application of the proposed algorithm are detailed. Finally, conclusions are given in Sect. VI. Throughout the paper, we use an italic letter to denote a scalar, a bold letter in lower case for a vector, and a capitalized bold letter[3] for a matrix.

II. Problem formulation

Let us consider the case as illustrated in Fig. 1 where the antenna array has M elements. The far-field propagation is generally assumed for the previous generation communication systems operating at the sub-6 GHz frequency and with a small element count M, i.e. a small array aperture. Under the assumption of plane wavefront, the directions of arrivals (DOAs) of the same propagation path at different array elements are the same. However, in the 5G mmWave communications and the corresponding propagation channel investigations, the element count M could be hundreds and even more than a thousand [2], [8], [15]. As a result, the Fraunhofer distance [35, Ch. 2.2.3]

$$d_{fr} = \frac{2D^2}{\lambda} \tag{1}$$

increases significantly, with D denoting the array aperture and λ the wavelength. This necessitates the consideration of spherical wavefront for a large-scale array in mmWave communications, since the plane wave assumption is considered reasonable only when the distance from the source point to the array is larger than the Fraunhofer distance.

In the underlying propagation channel model as illustrated in Fig. 1, we assume that totally L spherical-wave propagation paths impinge into the large-scale array. Referring to the selected reference point, the ℓth propagation path can be characterized by the propagation delay, azimuth, elevation, spherical distance and complex attenuation. We denote the parameter set as $\mathbf{\Gamma}_\ell = [\tau_\ell, \phi_\ell, \theta_\ell, d_\ell, \alpha_\ell]$. It is worth noting that d_ℓ represents the distance between the reference point and the spherical wavefront center observed by the array. d_ℓ is only directly related to τ_ℓ by light speed c as $d_\ell = c\tau_\ell$ for Line-of-Sight (LoS) path and Non-LoS (NLoS) paths with only specular reflections occurred along their propagation routes [12]. Otherwise, d_ℓ is less than the total propagating distance $c\tau_\ell$. In addition, α_ℓ is complex-valued due to the fact that a propagation path can experience phase shift and power decay along its propagation route.

The frequency response of the ℓth path $\mathbf{H}_\ell$ at the reference point is formatted as

$$\mathbf{H}_\ell(\mathbf{f}) = \alpha_\ell e^{-j2\pi \mathbf{f}\tau_\ell} \tag{2}$$

where $\mathbf{f}$ represents the frequency range[4]. In the case where the frequency range is discretely sampled with K frequency points, we define $\mathbf{f} = [f_1, \cdots, f_K]$. Therefore, $\mathbf{H}_\ell(\mathbf{f})$ is a complex-valued matrix with dimension of $1 \times K$, i.e. $\mathbf{H}_\ell(\mathbf{f}) \in \mathbb{C}^{1\times K}$. The spherical wavefront has two effects. One is that the phases of the mth element's responses change with respect to the reference point. The other is that the path power also changes due to the distance difference. Therefore, the frequency response of the ℓth path at the mth array element $\mathbf{H}_{m,\ell}(\mathbf{f}) \in \mathbb{C}^{1\times K}$ then reads

$$\mathbf{H}_{m,\ell}(\mathbf{f}) = r_m(\mathbf{d}_{m,\ell}) \frac{\| \mathbf{d}_\ell \|}{\| \mathbf{d}_{m,\ell} \|} e^{-j2\pi \mathbf{f} \frac{\|\mathbf{d}_{m,\ell}\| - \|\mathbf{d}_\ell\|}{c}} \odot \mathbf{H}_\ell(\mathbf{f}) \tag{3}$$

In (3), $\mathbf{d}_\ell$ represents the vector from the the last source point to the reference point. Specifically,

$$\mathbf{d}_\ell = -[d_\ell \sin\theta_\ell \cos\phi_\ell, d_\ell \sin\theta_\ell \sin\phi_\ell, d_\ell \cos\theta_\ell]^T \tag{4}$$

where $|\cdot|^T$ represents the transpose operation. $\mathbf{d}_{m,\ell}$ is the vector from the the source point to the mth array element, which is formatted as

$$\mathbf{d}_{m,\ell} = \mathbf{d}_\ell + \mathbf{d}_{mr} \tag{5}$$

where $\mathbf{d}_{mr}$ is the vector from the reference point to the mth array element that can be determined according to the array geometry. $\|\cdot\|$ denotes the Euclidean norm of the argument, $\odot$ represents the entry-wise product, and c denotes the light speed. Moreover, $r_m(\mathbf{d}_{m,\ell})$ indicates the extra response induced by the radiation pattern r_m of the mth array element in

[3]We also use a capitalized bold letter to denote a channel parameter vector, in which case the parameter vector can be considered as a matrix with a dimension as one.

[4]The mmWave propagation channel is usually measured by sweeping a frequency band using a vector network analyser (VNA) in most channel measurement campaigns. Thus, frequency response is exploited herein. In the case where channel impulse responses are measured in time domain, the frequency responses can be obtained by Fourier transform.

the direction of $\mathbf{d}_{m,\ell}$. The contribution of the ℓth path across the array can be expressed as

$$\mathbf{H}(\mathbf{f};\mathbf{\Gamma}_\ell) = [\mathbf{H}_{1,\ell},\cdots,\mathbf{H}_{M,\ell}]^T \tag{6}$$

where $\mathbf{H}(\mathbf{f};\mathbf{\Gamma}_\ell)$ is a complex-valued matrix with dimension of $M \times K$, i.e. $\mathbf{H}(\mathbf{f};\mathbf{\Gamma}_\ell) \in \mathbb{C}^{M\times K}$. The signal model in (6) assumes that the power is evenly distributed on the sphere wavefront. However, it can be violated due to the large array aperture. Among the other realistic propagation mechanisms, the scattering can lead to directive power lobe [36], and the array elements can be partially blocked. These effects can be much more obvious when the large-scale array is near to a scatterer causing directive lobe or a blocking object that cannot block all the elements. Although the spatial non-stationarity of the path gain at different array elements has been observed [15] in the literature, it has not been considered in the model assumption for the propagation parameter estimation as far as we are concerned. To more realistically describe the propagation channel, we propose a novel signal model based on (6) as

$$\mathbf{H}(\mathbf{f};\mathbf{\Theta}_\ell) = [\beta_{1,\ell}\mathbf{H}_{1,\ell},\cdots,\beta_{M,\ell}\mathbf{H}_{M,\ell}]^T \tag{7}$$

where $\mathbf{H}(\mathbf{f};\mathbf{\Theta}_\ell) \in \mathbb{C}^{M\times K}$, $\mathbf{\Theta}_\ell = [\mathbf{\Gamma}_\ell, \mathbf{B}_\ell]$, and $\mathbf{B}_\ell = [\beta_{1,\ell},\cdots,\beta_{M,\ell}]$ contains nonnegative real values. As an example, $\beta_{m,\ell} = 0$ means that the ℓth path is completely nonvisible to the mth element.

The array output reads

$$\mathbf{Y}(\mathbf{f}) = \sum_{\ell=1}^{L}\mathbf{H}(\mathbf{f};\mathbf{\Theta}_\ell) + \sqrt{\frac{\sigma^2}{2}}\mathbf{N}(\mathbf{f}) \tag{8}$$

where $\mathbf{N}(\mathbf{f})$ denotes the complex symmetric white Gaussian noise with both its real and imaginary parts as independent Gaussian variables of zero means and unit variances. For notation convenience, we further denote

$$\mathbf{H}(\mathbf{f};\mathbf{\Theta}) = \sum_{\ell=1}^{L}\mathbf{H}(\mathbf{f};\mathbf{\Theta}_\ell) \tag{9}$$

where $\mathbf{\Theta} = [\mathbf{\Theta}_1,\cdots,\mathbf{\Theta}_L]$ contains all the channel propagation parameters, which is of interest to be estimated.

III. Maximum likelihood based estimators

Estimators based on the ML principle can be derived to solve the problem defined in (8) given the empirically measured $\mathbf{Y}$. In the sequel, important ML-based estimators applied in the defined problem will be briefly discussed in terms of the basic principles and the limitations.

A. ML algorithm

The log-likelihood function of $\mathbf{\Theta}$ given the observation $\mathbf{Y}$ is formatted as [7], [32]

$$\Lambda(\mathbf{\Theta};\mathbf{Y}(\mathbf{f})) \triangleq -\frac{1}{\sigma^2} \parallel \mathrm{vec}\{\mathbf{Y}(\mathbf{f})\} - \mathrm{vec}\{\mathbf{H}(\mathbf{f};\mathbf{\Theta})\} \parallel^2 \tag{10}$$

where $\mathrm{vec}\{\cdot\}$ denotes the vectorization of the argument matrix. The ML estimation (MLE) results of Θ can be obtained by maximizing the log-likelihood function. That is,

$$\hat{\mathbf{\Theta}} = \arg\max_{\mathbf{\Theta}} \Lambda(\mathbf{\Theta};\mathbf{Y}) \tag{11}$$

However, the global maximum of Λ cannot be expressed in closed-form. The computation complexity is hence fatally high due to the high dimension ($[6+M]\,L$) of Θ, which prohibits its application in practice.[5]

B. EM algorithm

The expectation-maximization (EM) estimation [33], [37] is based on the operation that the incomplete data (i.e. the observable data $\mathbf{Y}$) can be decomposed into multiple (unobservable) complete data $\mathbf{C}(\mathbf{f};\mathbf{\Theta}_\ell)$ as

$$\mathbf{Y}(\mathbf{f};\mathbf{\Theta}) = \sum_{\ell=1}^{L}\mathbf{C}(\mathbf{f};\mathbf{\Theta}_\ell) \tag{12}$$

with

$$\mathbf{C}(\mathbf{f};\mathbf{\Theta}_\ell) = \mathbf{H}(\mathbf{f};\mathbf{\Theta}_\ell) + \sqrt{\frac{\omega_\ell\sigma^2}{2}}\mathbf{N}_\ell(\mathbf{f}) \tag{13}$$

where $\mathbf{N}_\ell$'s are independent complex symmetric white Gaussian noises have the same properties with $\mathbf{N}$ in (8), and the nonnegative ω_ℓ's meet $\sum_{\ell=1}^{L}\omega_\ell = 1$ for the decomposition of $\mathbf{N}$. The EM algorithm includes E-step and M-step. In the E-step, the conditional expectation of the log-likelihood of $\mathbf{\Theta}_\ell$ for $\mathbf{C}(\mathbf{f};\mathbf{\Theta}_\ell)$ is calculated, and the obtained log-likelihood is then maximized in the M-step. By iteratively updating parameters via E-steps and M-steps, the final EM estimation results $\hat{\mathbf{\Theta}}$ can be obtained. Specifically, in the E-step, the conditional expectation of the log-likelihood of $\mathbf{\Theta}_\ell$ given $\mathbf{Y}$ and assuming $\mathbf{\Theta} = \mathbf{\Theta}'$ is formatted as[6]

$$\Lambda(\mathbf{\Theta}_\ell;\hat{\mathbf{C}}(\mathbf{f};\mathbf{\Theta}'_\ell)) \triangleq -\frac{1}{\omega_\ell\sigma^2} \parallel \mathrm{vec}\{\hat{\mathbf{C}}(\mathbf{f};\mathbf{\Theta}'_\ell)\} - \mathrm{vec}\{\mathbf{H}(\mathbf{f};\mathbf{\Theta}_\ell)\} \parallel^2 \tag{14}$$

where $\hat{\mathbf{C}}(\mathbf{f};\mathbf{\Theta}'_\ell)$ denotes the conditional expectation of the complete data $\mathbf{C}(\mathbf{f};\mathbf{\Theta}_\ell)$ given $\mathbf{Y}$ and $\mathbf{\Theta}'$ that reads

$$\hat{\mathbf{C}}(\mathbf{f};\mathbf{\Theta}'_\ell) = \sqrt{\omega_\ell}\left[\mathbf{Y} - \mathbf{H}(\mathbf{f};\mathbf{\Theta}')\right] + \mathbf{H}(\mathbf{f};\mathbf{\Theta}'_\ell) \tag{15}$$

In the M-step, the log-likelihood is maximized as

$$\mathbf{\Theta}''_\ell = \arg\max_{\mathbf{\Theta}_\ell} \Lambda(\mathbf{\Theta}_\ell;\hat{\mathbf{C}}(\mathbf{f};\mathbf{\Theta}'_\ell)) \tag{16}$$

to update $\mathbf{\Theta}'_\ell$. Then $\mathbf{\Theta}''_\ell$ is exploited as $\mathbf{\Theta}'_\ell$ for the next iteration. Note that the proper initialization of $\mathbf{\Theta}'$ in the first iteration and the proper selection of ω_ℓ's can optimize the convergence [37]. By applying the EM principle, the $[6+M]\,L$ dimension problem can be decomposed into L separate $[6+M]$ problems plus iterations. Nevertheless, the computation complexity is still very high.

[5]The number "6" corresponds to τ_ℓ, ϕ_ℓ, θ_ℓ, d_ℓ and the real part and imaginary part of α_ℓ. The number M corresponds to the $\beta_{m,\ell}$'s.

[6]$\mathbf{\Theta}'$ is initialized as $\mathbf{\Theta}_0$ in the first iteration and then updated iteratively as the result obtained in the M-step of the previous iteration.

C. SAGE algorithm

Compared to the EM principle, the SAGE principle [32] mainly has two improvements. One is that it attempts to decompose the maximization problem (14) into multiple one-dimension maximization problems, e.g. in delay, angular and Doppler frequency domains, respectively. The decomposition is based on the assumption that the complete data $\mathbf{C}(\mathbf{f};\mathbf{\Theta}_\ell)$ contains multiple components (spaces) that follow orthogonal stochastic measures (OSM). The other improvement is that in each iteration, the SAGE principle exploits the already estimated MPC parameters immediately for calculating the expectation of the next path's complete data, while they are not updated until the next iteration in the EM principle. Readers are referred to Fig. 3 and Fig. 5 in [32] for an explicite comparison between EM and SAGE algorithms. The SAGE algorithm has been widely used in the propagation research in the past decades for its low computation complexity and faster convergence rate. However, in the ultra-wideband large-scale array systems, the narrowband assumption or the so-called small-scale assumption [7] is violated. Moreover, the large-scale aperture necessitates the consideration for the 3D spherical propagation (i.e. θ_ℓ and d_ℓ) and the spatial non-stationarity in path gain (i.e. $\beta_{m,\ell}$'s). The failure to design orthogonal spaces for parameters contained in $\mathbf{\Theta}$ opposes the application of SAGE. Nevertheless, investigations such as [15], [38] have been done by dividing the large-scale array into multiple small arrays or selecting a small fraction of the ultra-wide bandwidth to apply the SAGE algorithm, sacrificing the resolution and the large-scale array's ability in sensing the spherical propagation. Further, one propagation path could be presented in the form of a cluster when associating the channel characteristics observed at these small arrays, resulting in increased complexity yet decreased accuracy of channel models.

IV. The proposed TAMax algorithm

In this section, we propose a complexity-efficient estimator which is applicable for the problem formulated in Sect. II. The details of the proposed TAMax algorithm are presented in the sequel, where its low-complexity is also demonstrated and discussed.

A. Channel estimation at individual array elements

Let us revisit the frequency response at the mth array element contributed by the ℓth path. Considering the spatial non-stationarity in path gain, it can be re-written based on (3) as

$$\mathbf{H}_{m,\ell}(\mathbf{f}) = \alpha_{m,\ell} e^{-j2\pi \mathbf{f} \tau_{m,\ell}} \tag{17}$$

where

$$\alpha_{m,\ell} = \alpha_\ell \beta_{m,\ell} \frac{\parallel \mathbf{d}_\ell \parallel}{\parallel \mathbf{d}_{m,\ell} \parallel} r_m(\mathbf{d}_{m,\ell}) \tag{18}$$

and

$$\tau_{m,\ell} = \frac{\parallel \mathbf{d}_{m,\ell} \parallel - \parallel \mathbf{d}_\ell \parallel}{c} + \tau_\ell \tag{19}$$

For notation clarity, we denote $\mathbf{H}_{m,\ell}(\mathbf{f})$ as $\mathbf{H}_m(\mathbf{f};\mathbf{\Omega}_{m,\ell})$ with $\mathbf{\Omega}_{m,\ell} = [\alpha_{m,\ell}, \tau_{m,\ell}]$. The received signal $\mathbf{Y}_m(\mathbf{f}) \in \mathbb{C}^{1\times K}$ contributed by all the L paths at the mth array element then reads

$$\mathbf{Y}_m(\mathbf{f}) = \mathbf{H}_m(\mathbf{f};\mathbf{\Omega}_m) + \sqrt{\frac{\sigma^2}{2}} \mathbf{N}_m(\mathbf{f}) \tag{20}$$

where

$$\mathbf{H}_m(\mathbf{f};\mathbf{\Omega}_m) = \sum_{\ell=1}^{L} \mathbf{H}_m(\mathbf{f};\mathbf{\Omega}_{m,\ell}) \tag{21}$$

with $\mathbf{\Omega}_m = [\mathbf{\Omega}_{m,1}, \cdots, \mathbf{\Omega}_{m,L}]$, and $\mathbf{N}_m(f)$ denotes the complex symmetric white Gaussian noise with both its real and imaginary parts as independent Gaussian variables of zero means and unit variances. (21) demonstrates that at a specific array element, the propagation channel with L propagation paths can be represented by parameters $\alpha_{m,\ell}$'s and $\tau_{m,\ell}$'s. That is, the high dimension $\mathbf{\Theta}$ is compressed into the low dimension $\mathbf{\Omega}_m$ at this specific array element.

Given the empirically measured $\mathbf{Y}_m$, $\mathbf{\Omega}_m$ can be estimated according to the EM principle or SAGE principle. SAGE principle is exploited herein for its faster convergence rate. Specifically, in the E-step, $\hat{\mathbf{C}}_m(\mathbf{f};\mathbf{\Omega}'_{m,\ell})$ is calculated using (15) with $\mathbf{Y}$, $\mathbf{C}$, $\mathbf{H}$ and $\mathbf{\Theta}$ replaced with $\mathbf{Y}_m$, $\mathbf{C}_m$, $\mathbf{H}_m$ and $\mathbf{\Omega}_m$, respectively. Similarly, the M-step is formulated in (14) and (16) with $\mathbf{Y}$, $\mathbf{C}$, $\mathbf{H}$ and $\mathbf{\Theta}$ replaced with $\mathbf{Y}_m$, $\mathbf{C}_m$, $\mathbf{H}_m$ and $\mathbf{\Omega}_m$, respectively. Furthermore, considering the quasi-orthogonality among $\mathbf{H}_m(\mathbf{f};\mathbf{\Omega}_{m,\ell})$'s, the M-step in (14) can be approximated as

$$\tau'_{m,\ell} = \arg\max_{\tau} \mathrm{vec}\{\mathbf{H}_m(\mathbf{f};[1,\tau])\}^* \mathrm{vec}\{\hat{\mathbf{C}}_m(\mathbf{f};\mathbf{\Omega}'_{m,\ell})\} \tag{22}$$

where $(\cdot)^*$ represents Hermitian transpose of the argument. Then $\alpha'_{m,\ell}$ is obtained as

$$\alpha'_{m,\ell} = \frac{1}{K} \mathrm{vec}\{\mathbf{H}_m(\mathbf{f};[1,\tau'_{m,\ell}])\}^* \mathrm{vec}\{\hat{\mathbf{C}}_m(\mathbf{f};\mathbf{\Omega}'_{m,\ell})\} \tag{23}$$

Note that the superscripts of $\tau'_{m,\ell}$ and $\alpha'_{m,\ell}$ only have one "$\prime$" because they are updated immediately after the M-step in the SAGE principle.

It is intuitive that the complexity in estimating $\mathbf{\Omega}_m$ is low due to the low dimension order. Moreover, the accuracy is guaranteed by the SAGE principle. That is, the delay resolution can be as $1/5B$ with B denoting the bandwidth, which has been practically demonstrated in [32]. The estimation results for all the M array elements are denoted as $\hat{\mathbf{\Omega}} = [\hat{\mathbf{\Omega}}_1, \cdots, \hat{\mathbf{\Omega}}_M]$. The delays $\hat{\tau}_{m,\ell}$'s and complex attenuation coefficients $\hat{\alpha}_{m,\ell}$'s of the L paths estimated for individual array elements are written as rows in $\hat{\mathbf{\Omega}}^\tau \in \mathbb{R}^{M\times L}$ and $\hat{\mathbf{\Omega}}^\alpha \in \mathbb{C}^{M\times L}$, respectively for further processing.

B. Path trajectory identification

Thanks to the ultrawide bandwidth in the mmWave frequency bands, multiple propagation paths can be well separated in delay domain. Further, due to the large array aperture, the delay trajectory of one path, i.e. the variation of $\tau_{m,\ell}$, across the array element can also be observed. It is feasible to distinguish the multiple propagation paths by examining the trajectories in $\mathbf{\Omega}^\tau$. To effectively identify the trajectories of individual propagation paths, we propose a novel transform

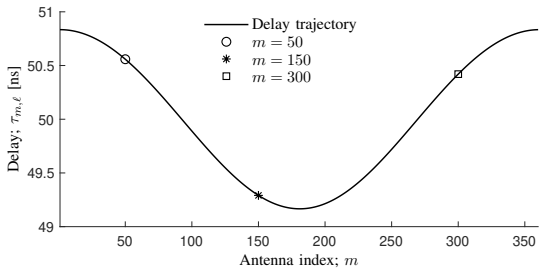

(a) Delay trajectory of one propagation path with geometry parameter set of $(50\,\text{ns}, 180°, 90°, 3\,\text{m})$ across a UCA. The UCA has 360 elements located on its perimeter of diameter of 0.5 m. The path delays at the 50, 150 and 300th elements are also indicated in this figure.

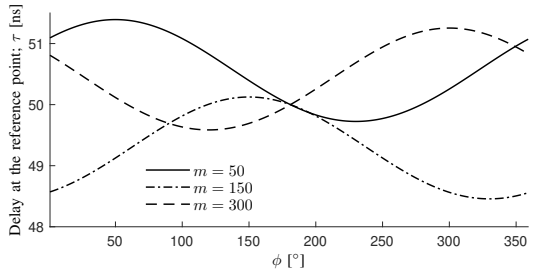

(b) The (τ, ϕ, θ, d) curves representing the countless delay trajectories that pass through the three points as indicated in Fig. 2(a), respectively. Parameters τ and ϕ of the path trajectory are solved by checking the intersection point. For illustration purpose, θ and d are fixed as 90° and 3 m respectively.

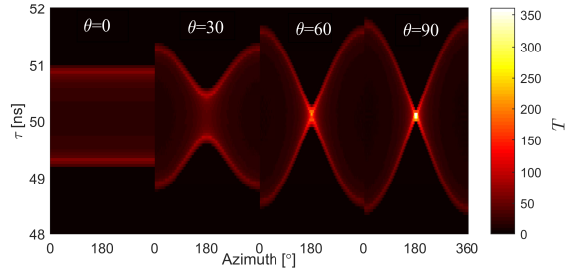

(c) The proposed transform (27)-(29) applied for the delay trajectory as illustrated in Fig. 2(a). τ_{th} is chosen as 0.075 ns to tolerate the dropping of d_ℓ, i.e. $d = +\infty$. This corresponds to $\frac{0.15}{B}$ with bandwidth B as 2 GHz, which is smaller than the delay resolution $\frac{1}{5B}$. For illustration purpose, ϕ is ranged from 0 to 360 degrees, and θ is ranged in (0, 30, 60, 90) degrees.

Fig. 2: An example illustration of the proposed transform.

for $\mathbf{\Omega}^\tau$. It is known from (19) that the delay trajectory of one propagation path across the elements is jointly determined by the geometrical parameters of the reference point, i.e., τ_ℓ, ϕ_ℓ, θ_ℓ and d_ℓ. In other words, given a path delay $\tau_{m,\ell}$ observed at the mth array element, there are countless delay trajectories that can pass through $\tau_{m,\ell}$, i.e., with their delays at the mth element equal $\tau_{m,\ell}$. These trajectories can be defined by different parameter sets (τ, ϕ, θ, d)'s observed at the reference center that meet

$$\tau = \tau_{m,\ell} - \frac{\parallel \mathbf{d}_{m,\ell} \parallel - \parallel \mathbf{d} \parallel}{c} \tag{24}$$

As an example, Fig. 2(a) illustrates a delay trajectory across the array elements of a UCA. Totally 360 array elements locate on the perimeter of diameter of 0.5 m, and the reference point is selected as the UCA center with geometry parameters $(\tau_\ell, \phi_\ell, \theta_\ell, d_\ell)$ as $(50\,\text{ns}, 180°, 90°, 3\,\text{m})$. Three delay points at the 50, 150 and 300th elements are also indicated in Fig. 2(a). For each of the three points, there are countless of possible trajectories that pass through it. Fig. 2(b) illustrates three curves in the (τ, ϕ, θ, d) domain that represent these countless delay trajectories passing through the three points, respectively. It can be observed from Fig. 2(b) that the three curves intersect at the point whose (τ, ϕ, θ, d) indicates the delay trajectory passing through the three points simultaneously. In fact, all the 360 curves in the (τ, ϕ, θ, d) domain that correspond to the 360 points in the $(\tau_{m,l}, m)$ domain intersect at this point. To count how many curves intersect at a specific point in (τ, ϕ, θ, d) domain, we propose to transform Ω^τ from $(\tau_{m,l}, m)$ domain to (τ, ϕ, θ, d) domain as

$$T(\tau, \phi, \theta, d; \Omega^\tau) = \sum_{m,\ell} \delta_{m,\ell}(\tau, \phi, \theta, d) \tag{25}$$

where

$$\delta_{m,\ell}(\tau, \phi, \theta, d) = \begin{cases} 1 & \text{if (24) holds} \\ 0 & \text{otherwise} \end{cases} \tag{26}$$

This way, by checking the maximum/maxima in $T(\tau, \phi, \theta, d)$, delay trajectory/trajectories can be identified. Specifically, in the example as illustrated in Fig. 2(c), the maximum of T can be found at $(50\,\text{ns}, 180°, 90°, 3\,\text{m})$ as 360. In addition, the maximum can be less than 360 if the path trajectory is totally blocked at some array elements.

However, the following facts for the empirically estimated $\hat{\Omega}^\tau$ need to be further considered. *i)* The estimated $\hat{\tau}_{m,\ell}$'s in $\hat{\Omega}^\tau$ are discrete; *ii)* The root-mean-square-errors between the estimated $\hat{\tau}_{m,\ell}$'s and the real delays are statistically bounded by the so-called Cramer-Rao lower bounds. Therefore, a delay threshold τ_{th} is involved to modify the proposed transform as

$$T(\tau, \phi, \theta; \hat{\mathbf{\Omega}}^\tau) = \sum_{m,\ell} \delta_{m,\ell}(\tau, \phi, \theta) \tag{27}$$

where

$$\delta_{m,\ell}(\tau, \phi, \theta) = \begin{cases} 1 & \text{if (29) holds with } d = +\infty \\ 0 & \text{otherwise} \end{cases} \tag{28}$$

with

$$|\hat{\tau}_{m,\ell} - \frac{\parallel \mathbf{d}_{m,\ell} \parallel - \parallel \mathbf{d} \parallel}{c} - \tau| \leq \tau_{th} \tag{29}$$

where $|\cdot|$ represents the absolute value of the argument. The delay trajectory that passes through the most number of $\hat{\tau}_{m,\ell}$'s can be identified as

$$(\tau'_\ell, \phi'_\ell, \theta'_\ell) = \arg\max_{\tau,\phi,\theta} T(\tau, \phi, \theta; \hat{\mathbf{\Omega}}^\tau) \tag{30}$$

The identified path trajectory is denoted as $\hat{\mathbf{\Omega}}_\ell$ ($\ell = 1$ denoting the first identified trajectory). The delay entries $\hat{\mathbf{\Omega}}_\ell^\tau$ in $\hat{\mathbf{\Omega}}^\tau$ and the corresponding attenuation entries $\hat{\mathbf{\Omega}}_\ell^\alpha$ in $\hat{\mathbf{\Omega}}^\alpha$ can be retrieved straightforward according to (30) and (29). To find the multiple delay trajectories of the multiple propagation paths, $\hat{\Omega}^\tau$ and $\hat{\Omega}^\alpha$ are updated respectively by removing $\hat{\Omega}_\ell^\tau$'s and $\hat{\Omega}_\ell^\alpha$'s that have been already identified, and the above

process repeats till no reasonable trajectory can be identified. The stop criterion is that the maximum of current T is below the pre-defined threshold M_{th}. Note that in (28)-(29) plane wave assumption ($d = +\infty$) is approximated to reduce computation complexity. The feasibility of the approximation is as follows: *i)* The "path trajectory identification" step is an intermediate estimation step. The objective is to identify trajectories of multiple propagation paths and obtain rough (rather than high-resolution) estimation results of their delays and angles. *ii)* Compared to the other geometry parameters, d_ℓ has an insignificant impact on the delay trajectory. In other words, the trajectory variation caused only by d_ℓ variation is insignificant, which is demonstrated by the simulation as illustrated in Fig. 2. It can be observed from Fig. 2(c) that it is fine to identify the trajectory with d omitted after introducing the tolerance τ_{th}, although the real d is rather small as 3 m. *iii)* It dose not mean that the spherical information has been omitted, though plane wave approximation is assumed in the trajectory identification. All the spherical information can be retrieved by exploiting the delays and complex amplitudes of path trajectories for high-resolution estimation as elaborated in Sect. IV-C.

In the above discussed trajectory identification step, the main computation load lies in (27)-(29), where filters as $\frac{\|\mathbf{d}\|-\|\mathbf{d}_m\|}{c}$ should be calculated for different parameter pairs, and then added (or subtracted) to each elements included in $\hat{\mathbf{\Omega}}^{\tau}$. Nevertheless, the filters can be calculated only once and stored to save computation source. Moreover, only in the first MPC trajectory identification, all the elements in $\hat{\mathbf{\Omega}}^{\tau}$ are involved to calculate T. For the following MPC trajectory identifications, one can calculate $T(\tau, \phi, \theta; \hat{\Omega}^{\tau}_{\ell-1})$ of the previous identified trajectory and subtract it from the current T to update T. Since the element number in $\hat{\Omega}^{\tau}_{\ell-1}$ is not large, the complexity is low. This is a strong advantage compared to the other classical techniques such as beamforming. In the beamforming techniques, power spectrum has to be recalculated for every iteration wherein a matrix with dimension $M \times K$ is always involved in multiplications and additions. Further, the interference among paths cannot be easily removed.

C. Estimation for the spherical propagation parameter $\mathbf{\Theta}_\ell$

For an identified $\hat{\mathbf{\Omega}}_\ell$, its estimated complete data $\hat{\mathbf{C}}(\mathbf{f}; \hat{\mathbf{\Omega}}_\ell)$ can be obtained using (17) with $\hat{\mathbf{\Omega}}^{\tau}_\ell$ and $\hat{\mathbf{\Omega}}^{\alpha}_\ell$. The propagation parameters τ_ℓ, ϕ_ℓ, θ_ℓ and d_ℓ can be estimated by solving the following 4D ML problem

$$\{\hat{\tau}_\ell, \hat{\phi}_\ell, \hat{\theta}_\ell, \hat{d}_\ell\} = \arg \max_{\tau,\phi,\theta,d} \text{vec}\{\mathbf{H}(\mathbf{f}; \mathbf{\Gamma}_a)\}^* \text{vec}\{\hat{\mathbf{C}}(\mathbf{f}; \hat{\mathbf{\Omega}}_\ell)\} \tag{31}$$

where $\mathbf{H}(\mathbf{f}; \mathbf{\Gamma}_a)$ is calculated using (6) with $\mathbf{\Gamma}_a = [\tau, \phi, \theta, d, 1]$. The complexity of the 4D searching is high. However, since only one propagation path is considered, we can decompose the 4D problem into a 3D problem and a 1D problem as follows. Firstly, ϕ_ℓ, θ_ℓ and d_ℓ can be estimated by solving the following 3D problem

$$\{\hat{\phi}_\ell, \hat{\theta}_\ell, \hat{d}_\ell\} = \arg \max_{\phi,\theta,d} \text{vec}\{\mathbf{H}(f_k; \mathbf{\Gamma}_b)\}^* \text{vec}\{\hat{\mathbf{C}}(f_k; \hat{\mathbf{\Omega}}_\ell)\} \tag{32}$$

where $\mathbf{H}(f_k; \mathbf{\Gamma}_b)$ is calculated using (6) with $\mathbf{\Gamma}_b = [0, \phi, \theta, d, 1]$, and f_k is a fixed frequency point. The low-complexity of this step lies in the facts that the searching space is significantly narrowed down referring to ϕ'_ℓ, θ'_ℓ and d'_ℓ ($d \le c\tau'_\ell$) obtained in (30), and that only one frequency point is exploited. Based on the estimation results $\{\hat{\phi}_\ell, \hat{\theta}_\ell, \hat{d}_\ell\}$, τ_ℓ is estimated by solving

$$\hat{\tau}_\ell = \arg \max_{\tau} \text{vec}\{\mathbf{H}(\mathbf{f}; \mathbf{\Gamma}_c)\}^* \text{vec}\{\hat{\mathbf{C}}(\mathbf{f}; \hat{\mathbf{\Omega}}_\ell)\} \tag{33}$$

where $\mathbf{\Gamma}_c = [\tau, \hat{\phi}_\ell, \hat{\theta}_\ell, \hat{d}_\ell, 1]$. The searching space of τ is also decreased significantly due to its initialization τ' in (30). With estimated geometry parameter set $\{\hat{\tau}_\ell, \hat{\phi}_\ell, \hat{\theta}_\ell, \hat{d}_\ell\}$, antenna radiation pattern and path loss effects can be easily removed from $\hat{\mathbf{\Omega}}^{\alpha}_\ell$. The complex attenuation coefficient $\hat{\alpha}_\ell$ is then chosen as the entry with the highest power in $\hat{\mathbf{\Omega}}^{\alpha}_\ell$. The parameter set $\hat{\mathbf{B}}_\ell$ can be determined as the element-wise ratio of $|\hat{\mathbf{\Omega}}^{\alpha}_\ell|$ to $|\hat{\alpha}_\ell|$.

D. Algorithm implementation procedure

The following pseudo-codes concisely summarize the implementation procedure of the proposed algorithm.[7]

Algorithm 1: Implementation procedure of the proposed algorithm:
Input: Empirically measured $\mathbf{Y}(\mathbf{f}) \in \mathbb{C}^{M \times K}$
Output: Channel propagation parameter $\mathbf{\Theta}$

```
Obtain Ω̂ (Ω̂^τ and Ω̂^α) at individual array elements
  according to Sect. IV-A;
Calculate T(τ, φ, θ) with Ω̂^τ according to (27)-(29);
Let ℓ = 1;
while True
  if ℓ > 1
    T = T − T(τ, φ, θ; Ω̂^τ_{ℓ−1});
  end if
  if T_max (the maximum of T) ≥ M_th
    Retrieve Ω̂_ℓ according to Sect. IV-B;
    Estimate Θ̂_ℓ from Ω̂_ℓ according to Sect. IV-C;
  else
    break;
  end if
  ℓ = ℓ + 1;
end while
```

V. Algorithm Application in Real Channels

In this section, a measurement campaign at the frequency band from 27 GHz to 29 GHz by using a UCA with radius of 0.25 m is introduced. Note that the proposed algorithm is generalized for an antenna array with arbitrary geometry. With available measurement facility in our case, a UCA is exploited. The application of the proposed TAMax algorithm and its performance in the real channels are presented and discussed.

[7]Readers can refer to [12], [32] for the Cramer-Rao-Lower-Bounds (statistical precision or performance which can be asymptotically achieved by a ML estimator) derived for plane-wavefront and spherical-wavefront cases, respectively.

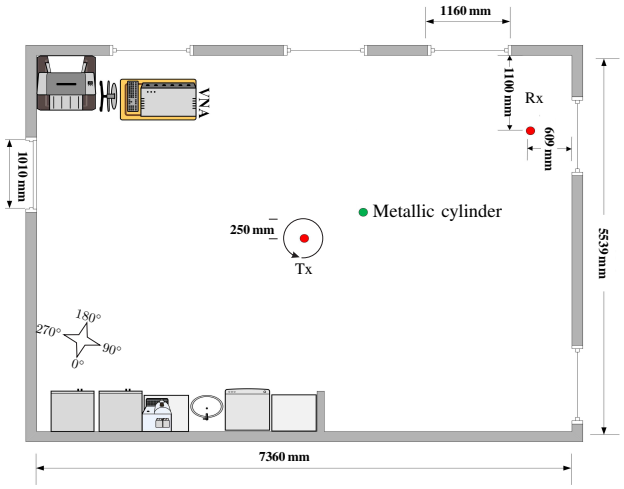

Fig. 3: The meeting room.

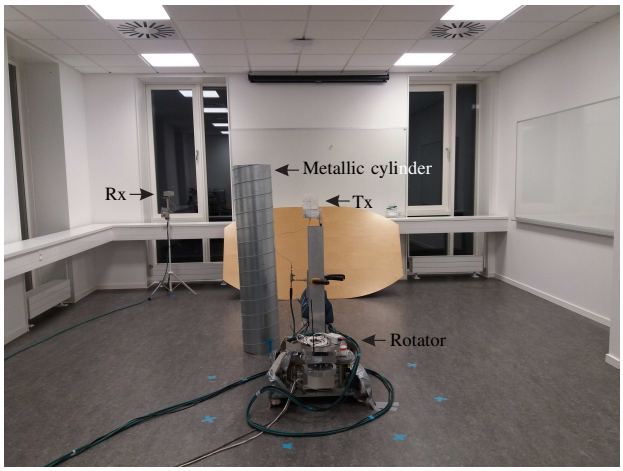

Fig. 4: A photo taken during the measurement preparation.

A. Measurement scenarios and specifications

The measurement campaign [39] was conducted in a meeting room of size 7.3 m×5.5 m as illustrated in Fig. 3 where the objects existing in the room are also indicated. Fig. 4 illustrates a photo taken during the measurement preparation. The transmitter (Tx) and receiver (Rx) were fixed at the locations as indicated in Fig. 3. The measurement system outlined in [40] based on a Vector Network Analyzer (VNA) was used to excite the propagation channel. The system swept the frequency range from 27 GHz to 29 GHz with 750 ($K = 750$) frequency points. That is, the frequency step was around 2.67 MHz which corresponds to a maximum observable delay of 375 ns and a maximum propagation distance of 112.5 m. In the Tx side, an omnidirectional antenna [41] was equipped on a rotator. The rotator was programmed to counterclockwise rotate the Tx antenna to different positions on the perimeter with radius of 0.25 m. The start position located at 0 degree as indicated in Fig. 3, and totally 360 ($M = 360$) rotation steps were performed to cover a circle. The distance between neighboring Tx positions of the formed virtual UCA was 4.4 mm. This is smaller than the half wavelength at 29 GHz so that the spatial

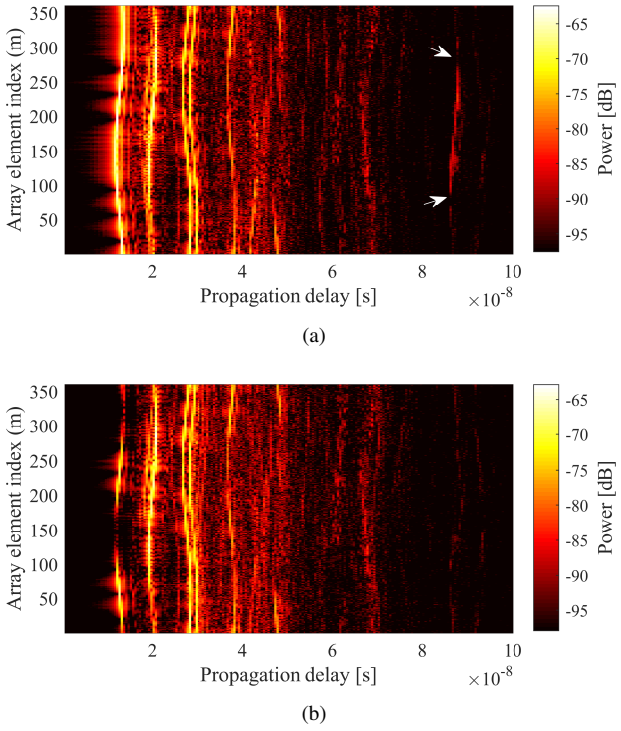

Fig. 5: CPDPs observed in the (a) LoS scenario and (b) OLoS scenario.

characteristics can be recorded without aliasing. The height of the Tx antenna to the floor was 1.3 m, and the transmitting power was set to 12 dBm. Another omnidirectional antenna (A-INFO-SZ-2003000/P) with the same height was exploited as the Rx antenna. The measurement was firstly carried out in the empty meeting room. Then the measurement was repeated with a hollow metallic cylinder placed at the green point as indicated in Fig. 3 with height of 1.55 m, diameter of 0.317 m and thickness of 1 mm. In the former case, the Rx was perfectly in the Line-of-Sight (LoS) of all the 360 virtual Tx positions. We denote this scenario as LoS scenario. In the latter case, due to the presence of the metallic cylinder, the LoS directions between the Rx and the Tx positions were partially blocked. The spatial non-stationarity of the LoS path gain across the array elements can be clearly observed. We denote this scenario as Obstructed-LoS (OLoS) scenario.

B. Empirically measured channels

To gain preliminary insights into the propagation characteristics, the channel impulse responses $\boldsymbol{y}(m, \tau)$'s were obtained by applying the Inverse Discrete Fourier Transform (IDFT) to the empirically measured $\mathbf{Y}(f)$'s in the two scenarios with respect to f. Fig. 5(a) and Fig 5(b) illustrate the Concatenated Power Delay Profiles (CPDPs), i.e. $|y(m, \tau)|^2$'s for the LoS scenario and OLoS scenario, respectively. The horizontal axis represents the propagation delay, the vertical axis denotes the array element index m, and the color indicates the received power in dB scale. It can be observed from both Fig. 5(a) and Fig 5(b) that multiple trajectories exist. It is obvious that the LoS path at

some array elements attenuate significantly due to the blockage of the metallic cylinder in the OLoS scenario. In the LoS scenario as illustrated in Fig. 5(a), spatial non-stationarity of path gain can also be observed obviously at some trajectories, e.g. the one indicated with white arrows. The patterns of these trajectories actually can reflect some information about the propagation characteristics. For example, the element index with the shortest delay in one trajectory can roughly indicate the azimuth, and the width of this trajectory spreading in delay domain can roughly indicate the elevation. Nevertheless, these trajectory are blurred in the delay domain, which is mainly due to the limited resolution and the sidelobes caused by the IDFT. To obtain the high-resolution estimation results of MPC parameters, the proposed algorithm, i.e. TAMax, is applied in the sequel.

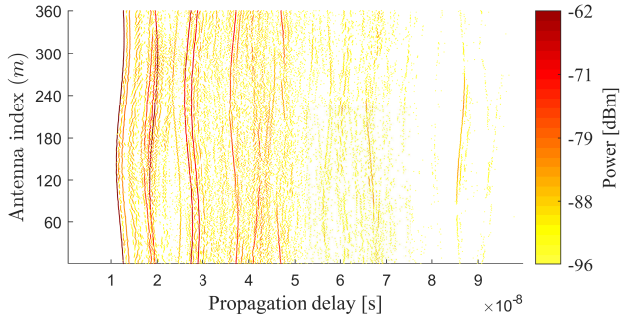

(a)

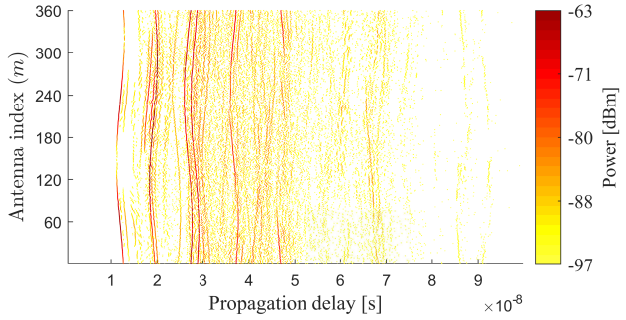

(b)

Fig. 6: $\hat{\Omega}$ estimated according to Sect. IV-A for the (a) LoS scenario and (b) OLoS scenario.

C. Algorithm application

Fig. 6(a) and Fig. 6(b) illustrate the estimated delays and complex amplitudes congregated at individual array elements (i.e. $\hat{\Omega}$) according to Sect. IV-A for the LoS scenario and OLoS scenarios, respectively. To fully extract the received power, the path number L should be sufficiently large. Generally, 30 dB of dynamic range is considered adequate to investigate the channel characteristics [42], [43]. Here, L is set as 60. It can be observed from Fig. 6(a) and Fig. 6(b) that the dynamic ranges are more than 30 dB. Benefiting from the high resolution, paths that are non-resolvable in the CPDP figures as illustrated in Fig. 5 are separated well in the delay domain in Fig. 6. Moreover, the spatial non-stationarity in path gain caused by the blockage is evident in the OLoS scenario, e.g. at the first-of-arrival path.

As detailed in Sect. IV-D, the path trajectory $\hat{\Omega}_\ell$ is then identified by exploiting the proposed transform in Sect. IV-B, and finally the spherical propagation parameters $\hat{\Theta}_\ell$ is estimated according to Sect. IV-C. As an example, Fig. 7 illustrates the procedure for estimating the propagation parameters of the first two paths in the OLoS scenario. In Fig. 7(a), the spectrum of the proposed transform for $\hat{\Omega}^\tau$ obtained in the OLoS scenario is presented, where the delay threshold τ_{th} is empirically chosen as $\frac{0.35}{B}$. This approximately corresponds to a propagation distance difference as 5 cm. Actually, two paths with propagation distance difference smaller than 5 cm can also be well distinguished in practice, because the angular parameters of the two paths are usually not the same. The global maximum of the spectrum is exploited to identify only one path, although multiple local maxima can be observed. This is because when a path trajectory in $\hat{\Omega}^\tau$ is transformed into the spectrum domain, sidelobes may exist as demonstrated in Fig. 2, which means that it is necessary to identify the multiple trajectories iteratively. By examining the spectrum maximum in Fig. 7(a), the first path $\hat{\Omega}_1^\tau$ is identified and indicated in blue in Fig. 7(b). As already discussed in Sect. IV-B, the complexity-efficient way is to subtract the spectrum of $\hat{\Omega}_1^\tau$ from the current spectrum of $\hat{\Omega}^\tau$ to obtain the residual spectrum, compared to recalculating it using $(\hat{\Omega}^\tau - \hat{\Omega}_1^\tau)$. The updated transform spectrum and the second path identified are presented in Fig. 7(c) and Fig. 7(d), respectively. The iterative procedure stops till the maximum of T is smaller than the pre-defined threshold M_{th} which is practically chosen as 150 for both LoS and OLoS scenarios in our case. Fig. 8(a) and Fig. 8(b) illustrate all the identified path trajectories indicated in different colors for the LoS scenario and OLoS scenario, respectively. We have the following observations. On one hand, the blockage of the metallic cylinder causes severe spatial non-stationarity in path gain, as more breaks can be observed in the OLoS trajectories. On the other hand, the spatial non-stationarity of path gain has no effect on the the proposed transform to identify these path trajectories, which gives advantage for further parameter extraction.

Based on these identified path trajectories, propagation parameters can be efficiently estimated according to Sect. IV-C. Fig. 9(a) and Fig. 9(b) illustrate the estimated delay-azimuth-power spectra for the LoS scenario and OLoS scenario, respectively. It can be clearly observed from Fig. 9 that the path constellations are basically similar in the two scenarios. Some paths, e.g. near to the LoS path, are disturbed by the metallic cylinder in the OLoS scenario. New paths, e.g. at the range around 30 ns delay and 150° azimuth, are also created in the OLoS scenario.

Fig. 10(a) and Fig. 10(b) illustrate the scatterer locations (spherical-wave centers) estimated in the LoS scenario and OLoS scenario, respectively. The shadow area indicates the office, the blue squares indicate the Rx and the UCA center, and the colored dots represent the scatterers whose locations are calculated by extending from the UCA center a length

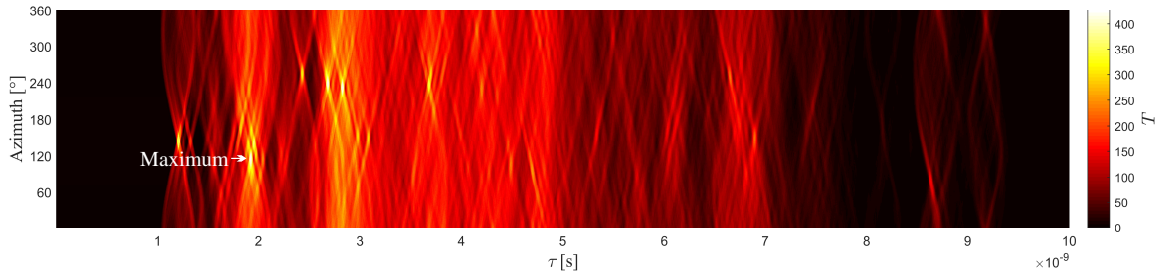

(a) The spectrum of the proposed transform for $\hat{\Omega}^{\tau}$

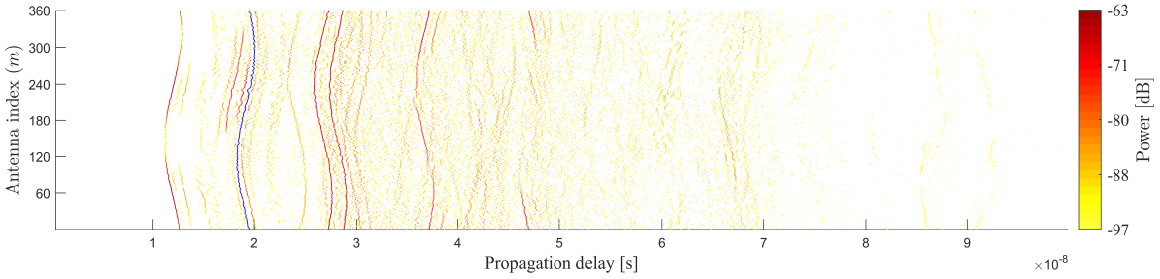

(b) Identified path trajectory $\hat{\Omega}_1^{\tau}$ (in blue) referring to the maximum of the spectrum in Fig. 7(a)

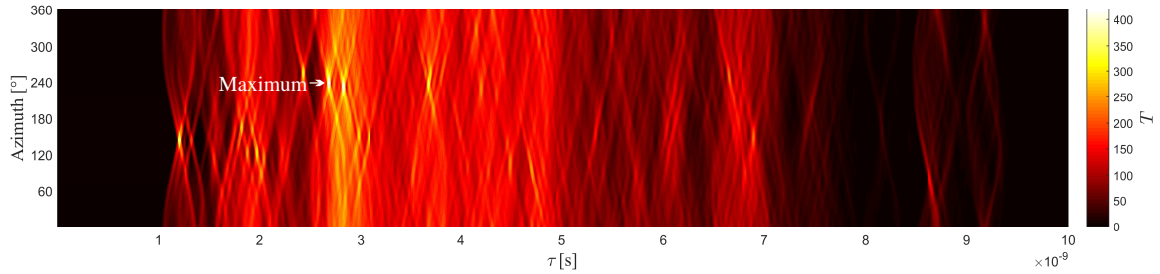

(c) The spectrum of the proposed transform for $\hat{\Omega}^{\tau}$ with the first path $\hat{\Omega}_1^{\tau}$ removed

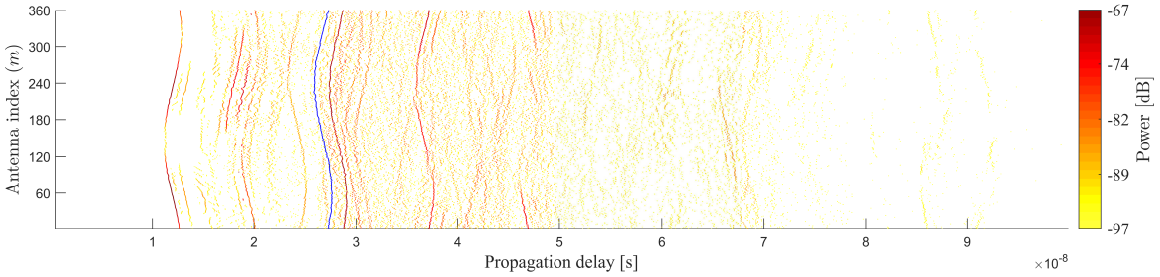

(d) Identified path trajectory $\hat{\Omega}_2^{\tau}$ (in blue) referring to the maximum of the spectrum in Fig. 7(c). The first path is also removed (not plotted) herein.

Fig. 7: Illustration of the estimation procedure for the first two paths in the OLoS scenario. Since the maxima that correspond to the first two path are found in the spectrum with $\theta = 90°$, the spectrum part with other elevations are not illustrated in Fig. 7(a) and Fig. 7(a) for clarity.

of estimated spherical distance along the estimated angular direction. A location in Fig. 10 indicates the real scatterer location, e.g. the antenna point or a point on a rough surface, that not only serves as the last-hop point but also with scattering happens there; whereas if a specular reflection happens at the last-hop point of the propagation path, the location indicates the mirror location of the real scattering point, in which case the illustrated location will be located outside the office. It can be observed from Fig. 10(a) that scatterers are located near to the Rx point in the LoS scenario. This is reasonable since that the antenna emits LoS spherical waves that can be perfectly received without blockage, and that the signals interacting with the top-right corner of the room were not blocked, either. It also makes sense that some scatterers near to the walls and furniture inside the room. Moreover, some scatterers are also estimated outside the room due to the fact that specular reflections can happen in the room. In the OLoS scenario as illustrated in Fig. 10(b), scatterer located exactly in the Rx point disappears, because part of the array elements are blocked or disturbed by the metallic cylinder so that the estimation accuracy for the LoS path is decreased. The scatterer number near to the left-bottom corner of the room also

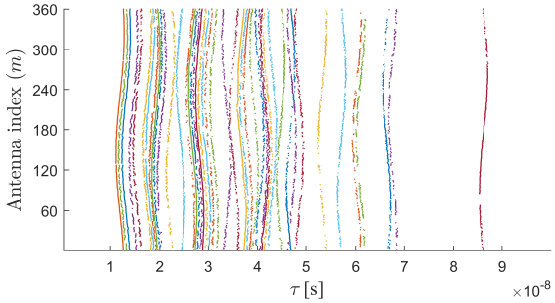

(a) LoS scenario with 46 paths identified

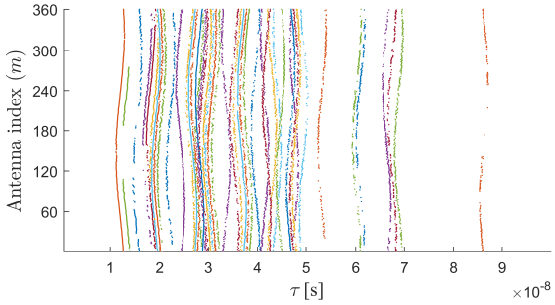

(b) OLoS scenario with 44 paths identified

Fig. 8: Identified $\hat{\Omega}_\ell^\tau$'s indicated in different color for (a) LoS scenario and (b) OLoS scenario.

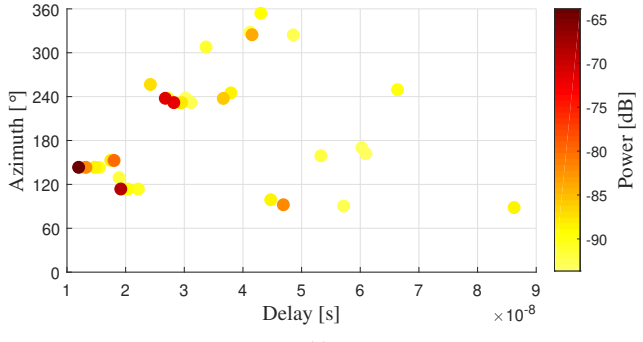

(a)

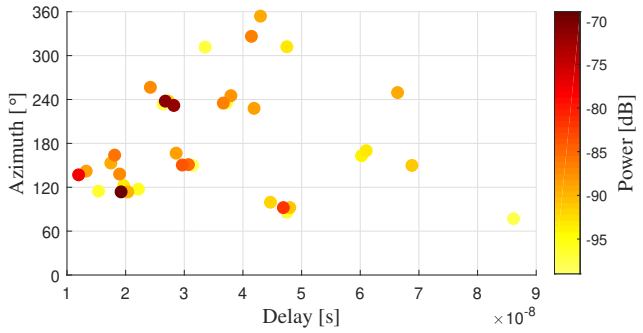

(b)

Fig. 9: Delay-azimuth-power spectra estimated using TAMax algorithm. (a) LoS scenario with 35 paths in 30 dB dynamic range. (b) OLoS scenario with 36 paths in 30 dB dynamic range.

decreases due to the blockage. Furthermore, it is interesting to observe that scatterers near to the metallic cylinder are newly born in the OLoS scenario. This is consistent with the fact that signal interacting with the round wall of the cylinder can create new paths.

D. Results Comparison with EM principle

Fig. 11(a) and Fig. 11(b) illustrate the estimated delay-azimuth-power spectra for both LoS and OLoS cases by using the EM principle[8] as elaborated in Sect. III-B. Note that the spatial non-stationarity in path gain cannot be considered in the EM principle, i.e., $\mathbf{B}_\ell = \mathbf{1}$ is set for all paths in the EM estimation. By comparing Fig. 9 and Fig. 11, it can be observed that the spectrum patterns are similar. Meanwhile, advantages of the proposed TAMax algorithm in decreasing complexity and obtaining more practical results can also be observed as follows. *i)* Many more paths are estimated by using the EM principle for the same 30 dB dynamic range. This is because when assuming stationary path gain, several paths are estimated to constitute one practical path with non-stationary path gain. An evident example is indicated in Fig 11(b) where 4 paths were estimated for the partially blocked LoS path in the OLoS scenario. *ii)* Some paths that can be sensed in the TAMax estimation are omitted in the EM estimation. This

[8]It is noteworthy that in the MATLAB environment and with the same quantization interval for the final estimation results, the runtime of the EM algorithm was several hours, while the runtime of the proposed TAMax algorithm was less than 3 minutes. This quantitatively demonstrates the low-complexity of the proposed algorithm by exploiting the strategies avoiding high dimensional joint-estimation and finding good initialization points.

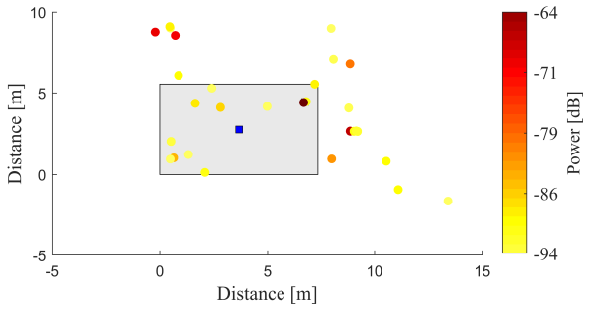

(a)

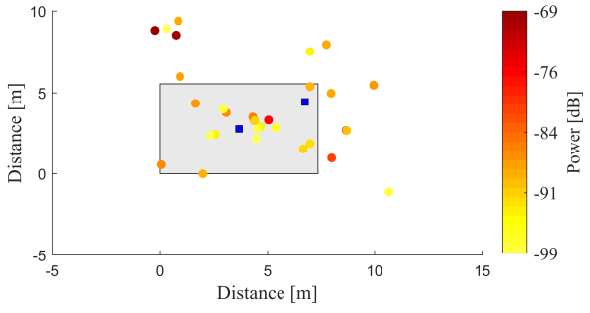

(b)

Fig. 10: Scatterers estimated using TAMax algorithm. (a) LoS scenario. (b) OLoS scenario.

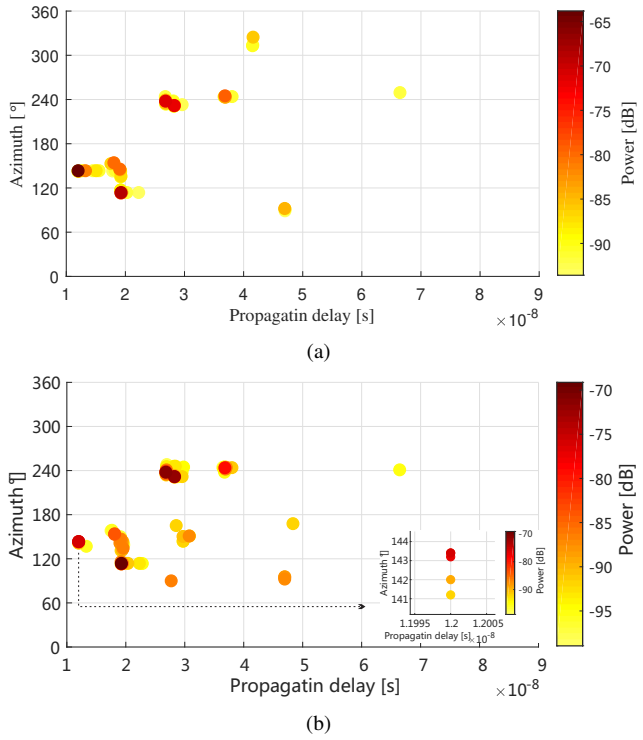

Fig. 11: Delay-azimuth-power spectra estimated using EM algorithm. (a) LoS scenario with 63 paths in 30 dB dynamic range. (b) OLoS scenario with 87 paths in 30 dB dynamic range.

is because the EM principle cannot account the spatial non-stationarity in path gain. For those paths with relatively small power and also with severe non-stationarity in path gain, e.g. with half of the array elements totally blocked. The power of its likelihood function (14) in EM will be further decreased by assuming that all the array element can received signals perfectly.

VI. Conclusions

In this contribution, a realistic spherical-propagation signal model was proposed for ultra-wideband large-scale array systems, where the spatial non-stationarity of path gain across the array was also considered. The state-of-the-art High-Resolution propagation Parameter Estimation (HRPE) algorithms were revisited, where prohibitive computation load or unrealistic assumptions hinder their applications. To overcome the issues, a novel HRPE algorithm, i.e. Trajectory-Aided Maximum-likelihood (TAMax), was proposed and then applied in a measurement campaign which was conducted in an office room with line-of-sight and obstructed-line-of-sight propagation scenarios designed. The accuracy and low-complexity of TAMax algorithm was demonstrated in theoretical and practical aspects. Whereas the increased bandwidth and increased aperture in the mmWave massive Multiple-Input-Multiple-Output (MIMO) systems bring pains to the existing estimation algorithms, TAMax algorithm can take them as advantages. By exploiting the ultra-wide bandwidth and the large-scale array aperture, high-resolution trajectories can be used to acquire interference cancellation and fast initialization. The results demonstrated that the proposed TAMax algorithm is able to obtain high-resolution estimation results of the spherical propagation channel in a complexity-efficient way. Further, by considering the spatial non-stationarity in path gain, the TAMax is more powerful to obtain realistic results and to detect weak paths. Future work will exploit TAMax for comprehensive and accurate mmWave massive MIMO channel modeling in various propagation environments.

VII. Acknowledgment

The authors wish to express their thanks to Mr. A. W. Mbugua and Dr. K. Saito for conducting the measurement. The work was partially supported by Huawei technologies, InnoExplorer project (2019 9122-00089A) funded by Innovation Fund Denmark and China National Science Fundation (CNSF) general project with grant number 61971313.

References

[1] J. G. Andrews, S. Buzzi, W. Choi, S. V. Hanly, A. Lozano, A. C. K. Soong, and J. C. Zhang, "What will 5G be?" *IEEE Journal on Selected Areas in Communications*, vol. 32, no. 6, pp. 1065–1082, June 2014.

[2] M. Shafi, A. F. Molisch, P. J. Smith, T. Haustein, P. Zhu, P. D. Silva, F. Tufvesson, A. Benjebbour, and G. Wunder, "5G: A tutorial overview of standards, trials, challenges, deployment, and practice," *IEEE Journal on Selected Areas in Communications*, vol. 35, no. 6, pp. 1201–1221, June 2017.

[3] T. S. Rappaport, S. Sun, R. Mayzus, H. Zhao, Y. Azar, K. Wang, G. N. Wong, J. K. Schulz, M. Samimi, and F. Gutierrez, "Millimeter wave mobile communications for 5G cellular: It will work!" *IEEE Access*, vol. 1, pp. 335–349, 2013.

[4] S. Rangan, T. S. Rappaport, and E. Erkip, "Millimeter-wave cellular wireless networks: Potentials and challenges," *Proceedings of the IEEE*, vol. 102, no. 3, pp. 366–385, March 2014.

[5] R. He, B. Ai, G. L. Stüber, G. Wang, and Z. Zhong, "Geometrical-based modeling for millimeter-wave MIMO mobile-to-mobile channels," *IEEE Transactions on Vehicular Technology*, vol. 67, no. 4, pp. 2848–2863, April 2018.

[6] A. L. Swindlehurst, E. Ayanoglu, P. Heydari, and F. Capolino, "Millimeter-wave massive MIMO: the next wireless revolution?" *IEEE Communications Magazine*, vol. 52, no. 9, pp. 56–62, September 2014.

[7] H. Krim and M. Viberg, "Two decades of array signal processing research: the parametric approach," *IEEE Signal Processing Magazine*, vol. 13, no. 4, pp. 67–94, Jul 1996.

[8] S. A. Busari, K. M. S. Huq, S. Mumtaz, L. Dai, and J. Rodriguez, "Millimeter-wave massive MIMO communication for future wireless systems: A survey," *IEEE Communications Surveys Tutorials*, vol. 20, no. 2, pp. 836–869, Secondquarter 2018.

[9] V. Jungnickel, K. Manolakis, W. Zirwas, B. Panzner, V. Braun, M. Lossow, M. Sternad, R. Apelfrojd, and T. Svensson, "The role of small cells, coordinated multipoint, and massive MIMO in 5G," *IEEE Communications Magazine*, vol. 52, no. 5, pp. 44–51, May 2014.

[10] V. Raghavan, L. Akhoondzadeh-Asl, V. Podshivalov, J. Hulten, M. A. Tassoudji, O. H. Koymen, A. Sampath, and J. Li, "Statistical blockage modeling and robustness of beamforming in millimeter-wave systems," *IEEE Transactions on Microwave Theory and Techniques*, vol. 67, no. 7, pp. 3010–3024, July 2019.

[11] S. Zhang, T. Jost, R. Pöhlmann, A. Dammann, D. Shutin, and P. A. Hoeher, "Spherical wave positioning based on curvature of arrival by an antenna array," *IEEE Wireless Communications Letters*, vol. 8, no. 2, pp. 504–507, April 2019.

[12] X. Yin, S. Wang, N. Zhang, and B. Ai, "Scatterer localization using large-scale antenna arrays based on a spherical wave-front parametric model," *IEEE Transactions on Wireless Communications*, vol. 16, no. 10, pp. 6543–6556, Oct 2017.

[13] E. D. Carvalho, A. Ali, A. Amiri, M. Angjelichinoski, and R. W. H. Jr, "Non-stationarities in extra-large scale massive MIMO," arXiv:1903.03085, 2019.

[14] Y. Ji, W. Fan, and G. F. Pedersen, "Channel characterization for wideband large-scale antenna systems based on a low-complexity maximum likelihood estimator," *IEEE Transactions on Wireless Communications*, vol. 17, no. 9, pp. 6018–6028, Sep. 2018.

[15] J. Chen, X. Yin, X. Cai, and S. Wang, "Measurement-based massive MIMO channel modeling for outdoor LoS and NLoS environments," *IEEE Access*, vol. 5, pp. 2126–2140, 2017.

[16] S. Singh, F. Ziliotto, U. Madhow, E. Belding, and M. Rodwell, "Blockage and directivity in 60 GHz wireless personal area networks: from cross-layer model to multihop MAC design," *IEEE Journal on Selected Areas in Communications*, vol. 27, no. 8, pp. 1400–1413, October 2009.

[17] A. Loch, I. Tejado, and J. Widmer, "Potholes ahead: Impact of transient link blockage on beam steering in practical mm-wave systems," in *European Wireless 2016; 22th European Wireless Conference*, May 2016, pp. 1–6.

[18] V. Raghavan, A. Partyka, A. Sampath, S. Subramanian, O. H. Koymen, K. Ravid, J. Cezanne, K. Mukkavilli, and J. Li, "Millimeter-wave MIMO prototype: Measurements and experimental results," *IEEE Communications Magazine*, vol. 56, no. 1, pp. 202–209, Jan 2018.

[19] C. Ling, X. Yin, R. Müller, S. Häfner, D. Dupleich, C. Schneider, J. Luo, H. Yan, and R. Thomä, "Double-directional dual-polarimetric cluster-based characterization of 70-77 GHz indoor channels," *IEEE Transactions on Antennas and Propagation*, vol. 66, no. 2, pp. 857–870, Feb 2018.

[20] C. Ling, X. Yin, H. Wang, and R. S. Thomä, "Experimental characterization and multipath cluster modeling for 13-17 GHz indoor propagation channels," *IEEE Transactions on Antennas and Propagation*, vol. 65, no. 12, pp. 6549–6561, Dec 2017.

[21] S. Hur, S. Baek, B. Kim, Y. Chang, A. F. Molisch, T. S. Rappaport, K. Haneda, and J. Park, "Proposal on millimeter-wave channel modeling for 5G cellular system," *IEEE Journal of Selected Topics in Signal Processing*, vol. 10, no. 3, pp. 454–469, April 2016.

[22] T. S. Rappaport, G. R. MacCartney, M. K. Samimi, and S. Sun, "Wideband millimeter-wave propagation measurements and channel models for future wireless communication system design," *IEEE Transactions on Communications*, vol. 63, no. 9, pp. 3029–3056, Sept 2015.

[23] F. Zhang, W. Fan, and G. F. Pedersen, "Frequency-invariant uniform circular array for wideband mm-wave channel characterization," *IEEE Antennas and Wireless Propagation Letters*, vol. 16, pp. 641–644, 2017.

[24] A. Liao, Z. Gao, Y. Wu, H. Wang, and M. Alouini, "2D unitary ESPRIT based super-resolution channel estimation for millimeter-wave massive MIMO with hybrid precoding," *IEEE Access*, vol. 5, pp. 24 747–24 757, 2017.

[25] F. Gao and A. B. Gershman, "A generalized ESPRIT approach to direction-of-arrival estimation," *IEEE Signal Processing Letters*, vol. 12, no. 3, pp. 254–257, March 2005.

[26] A. . van der Veen, M. C. Vanderveen, and A. J. Paulraj, "Joint angle and delay estimation using shift-invariance properties," *IEEE Signal Processing Letters*, vol. 4, no. 5, pp. 142–145, May 1997.

[27] C. Tsai, Y. Liu, and A. Wu, "Efficient compressive channel estimation for millimeter-wave large-scale antenna systems," *IEEE Transactions on Signal Processing*, vol. 66, no. 9, pp. 2414–2428, May 2018.

[28] M. C. Vanderveen, C. B. Papadias, and A. Paulraj, "Joint angle and delay estimation (JADE) for multipath signals arriving at an antenna array," *IEEE Communications Letters*, vol. 1, no. 1, pp. 12–14, Jan 1997.

[29] Z. Marzi, D. Ramasamy, and U. Madhow, "Compressive channel estimation and tracking for large arrays in mm-wave picocells," *IEEE Journal of Selected Topics in Signal Processing*, vol. 10, no. 3, pp. 514–527, April 2016.

[30] X. Li, J. Fang, H. Li, and P. Wang, "Millimeter wave channel estimation via exploiting joint sparse and low-rank structures," *IEEE Transactions on Wireless Communications*, vol. 17, no. 2, pp. 1123–1133, Feb 2018.

[31] S. Sun, T. S. Rappaport, M. Shafi, P. Tang, J. Zhang, and P. J. Smith, "Propagation models and performance evaluation for 5G millimeter-wave bands," *IEEE Transactions on Vehicular Technology*, vol. 67, no. 9, pp. 8422–8439, Sept 2018.

[32] B. H. Fleury, M. Tschudin, R. Heddergott, D. Dahlhaus, and K. I. Pedersen, "Channel parameter estimation in mobile radio environments using the SAGE algorithm," *IEEE Journal on Selected Areas in Communications*, vol. 17, no. 3, pp. 434–450, Mar 1999.

[33] T. Moon, "The expectation-maximization algorithm," *IEEE Signal Processing Magazine*, 1997.

[34] X. Cai and W. Fan, "A complexity-efficient high resolution propagation parameter estimation algorithm for ultra-wideband large-scale uniform circular array," *IEEE Transactions on Communications*, vol. 67, no. 8, pp. 5862–5874, Aug 2019.

[35] C. A. Balanis, *Antenna theory: analysis and design*. 3rd ed. Hoboken, NJ, USA: Wiley, 2005.

[36] V. Degli-Esposti, F. Fuschini, E. M. Vitucci, and G. Falciasecca, "Measurement and modelling of scattering from buildings," *IEEE Transactions on Antennas and Propagation*, vol. 55, no. 1, pp. 143–153, Jan 2007.

[37] M. Feder and E. Weinstein, "Parameter estimation of superimposed signals using the EM algorithm," *IEEE Transactions on Acoustics, Speech, and Signal Processing*, vol. 36, no. 4, pp. 477–489, April 1988.

[38] C. Gustafson, K. Haneda, S. Wyne, and F. Tufvesson, "On mm-wave multipath clustering and channel modeling," *IEEE Transactions on Antennas and Propagation*, vol. 62, no. 3, pp. 1445–1455, March 2014.

[39] A. W. Mbugua, K. Saito, F. Zhang, and W. Fan, "Characterization of human body shadowing in measured millimeter-wave indoor channels," in *IEEE 29th Annual International Symposium on Personal, Indoor and Mobile Radio Communications (PIMRC)*, Sep. 2018, pp. 1–5.

[40] J. Hejselbaek, Y. Ji, W. Fan, and G. F. Pedersen, "Channel sounding system for mm-wave bands and characterization of indoor propagation at 28 GHz," *International Journal of Wireless Information Networks*, vol. 24, no. 3, pp. 204–216, Sep 2017.

[41] S. S. Zhekov, A. Tatomirescu, and G. F. Pedersen, "Antenna for ultra-wideband channel sounding," *IEEE Antennas and Wireless Propagation Letters*, vol. 16, pp. 692–695, 2017.

[42] M. K. Samimi and T. S. Rappaport, "3-D millimeter-wave statistical channel model for 5G wireless system design," *IEEE Transactions on Microwave Theory and Techniques*, vol. 64, no. 7, pp. 2207–2225, July 2016.

[43] M. Martinez-Ingles, D. P. Gaillot, J. Pascual-Garcia, J. Molina-Garcia-Pardo, M. Lienard, and J. Rodríguez, "Deterministic and experimental indoor mmW channel modeling," *IEEE Antennas and Wireless Propagation Letters*, vol. 13, pp. 1047–1050, 2014.

Xuesong Cai received the B.S. degree and the Ph.D. degree (Hons.) from Tongji University, Shanghai, China, in 2013 and 2018, respectively. In 2015, he conducted a three-month internship with Huawei Technologies, Shanghai, China. He was also a Visiting Scholar with Universidad Politécnica de Madrid, Madrid, Spain in 2016. From 2018-2020, he was a postdoctoral research fellow with the APMS section, Department of Electronic Systems, Aalborg University (AAU), Aalborg, Denmark. Since April 2020, he has been a postdoctoral fellow with the Wireless Communication Networks Section, Department of Electronic Systems, AAU, cooperating with Nokia Bell Labs. His research interests include propagation channel measurement, high-resolution parameter estimation, channel characterization, channel modeling and over-the-air testing for wireless communications.

Dr. Cai was a recipient of the Chinese National Scholarship for Ph.D. Candidates and Excellent Student award in 2016, the Excellent Student award and the "ZTE Fantastic Algorithm" award in 2017, the Outstanding Doctorate Graduate awarded by Shanghai Municipal Education Commission and "ZTE Blue Sword-Future Leaders Plan" in 2018, and the "Seal of Excellence" with the European Horizon 2020's Marie Skłodowska-Curie actions call in 2019.

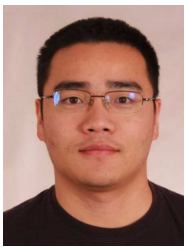

Wei Fan received his Bachelor of Engineering degree from Harbin Institute of technology, China in 2009, Master's double degree with highest honours from Politecnico di Torino, Italy and Grenoble Institute of Technology, France in 2011, and Ph.D. degree from Aalborg University, Denmark in 2014. From February 2011 to August 2011, he was with Intel Mobile Communications, Denmark as a research intern. He conducted a three-month internship at Anite telecoms oy (now Keysight technologies), Finland in 2014. His main areas of research are over-the-air testing of multiple antenna systems, radio channel sounding, modeling and emulation, and antenna array signal processing. He is currently an associate professor at the Antennas, Propagation and Millimeter-wave Systems (APMS) Section at Aalborg University.

Xuefeng Yin (S'01–M'06) received the Bachelor's degree in optoelectronics engineering from Huazhong University of Science and Technology, Wuhan, China, in 1995, and the Master of Science degree in digital communications and the Ph.D. in wireless communications from Aalborg University, Aalborg, Denmark, in 2002 and 2006, respectively. From 2006 to 2008, he was an Assistant Professor with Aalborg University. In 2008, he joined the College of Electronics and Information Engineering, Tongji University, Shanghai, China. He became a Full Professor in 2016 and has been the Vice Dean of the college since then. His research interests include high-resolution parameter estimation for propagation channels, measurement-based channel characterization and stochastic modeling for 5G wireless communications, channel simulation based on random graph models, radar signal processing, and target recognition. He has authored or coauthored more than 130 technical papers and coauthored the book Propagation Channel Characterization, Parameter Estimation and Modeling for Wireless Communications (Wiley, 2016).

Gert Frølund Pedersen was born in 1965. He received the B.Sc. and E.E. (Hons.) degrees in electrical engineering from the College of Technology in Dublin, Dublin Institute of Technology, Dublin, Ireland, in 1991, and the M.Sc.E.E. and Ph.D. degrees from Aalborg University, Aalborg, Denmark, in 1993 and 2003, respectively. Since 1993, he has been with Aalborg University where he is a Full Professor heading the Antennas, Propagation and Millimeter-wave Systems LAB with 25 researchers. He is also the Head of the Doctoral School on wireless communication with some 40 Ph.D. students enrolled. His research interests include radio communication for mobile terminals especially small antennas, diversity systems, propagation, and biological effects. He has published more than 500 peer reviewed papers, 6 books, 12 book chapters and holds over 50 patents. He has also worked as a Consultant for developments of more than 100 antennas for mobile terminals including the first internal antenna for mobile phones in 1994 with lowest SAR, first internal triple-band antenna in 1998 with low SAR and high TRP and TIS, and lately various multiantenna systems rated as the most efficient on the market. He has worked most of the time with joint university and industry projects and have received more than 21 M$ in direct research funding. He is currently the Project Leader of the RANGE project with a total budget of over 8 M$ investigating high performance centimetre/millimetre-wave antennas for 5G mobile phones. He has been one of the pioneers in establishing over-the-air measurement systems. The measurement technique is now well established for mobile terminals with single antennas and he was chairing the various COST groups with liaison to 3GPP and CTIA for over-the-air test of MIMO terminals. He is currently involved in MIMO OTA measurement.